Supporting information

Computational demonstration of Isomer- and spin-state-dependent charge transport in molecular junctions composed of charge-neutral iron(II) spin-crossover complexes

Nicolás Montenegro-Pohlhammer,[a,b]* Senthil Kumar Kuppusamy,[c]* Gloria Cárdenas-Jirón,[a] Carmen J. Calzado[b] and Mario Ruben[c,d,e]

[a]Laboratory of Theoretical Chemistry, Faculty of Chemistry and Biology, University of Santiago de Chile (USACH), 9170022, Santiago, Chile.

[b]Departamento de Química Física. Universidad de Sevilla. c/ Profesor García González, s/n. 41012 Sevilla. Spain.

[c]Institute for Quantum Materials and Technologies (IQMT), Karlsruhe Institute of Technology (KIT), Karlsruhe, Germany.

[d]Institute of Nanotechnology, Karlsruhe Institute of Technology (KIT), Karlsruhe, Germany.

[e]Centre Européen de Sciences Quantiques (CESQ), Institut de Science et d'Ingénierie Supramoléculaire (ISIS), Université de Strasbourg, Strasbourg, France.

*Authors to whom the correspondence should be addressed

Email: nicolas.montenegro.p@usach.cl, senthil.kuppusamy2@kit.edu.

Contents

S1. Synthesis of ligands and complexes

S1.1. Synthesis of L1 and complex 1

Complex 1 was synthesized from the previously reported 5,5'-diethynyl-2,2'-bipyridine[1] precursor as depicted in scheme 1. Complex 1 was obtained as a greenish-yellow precipitate with about 16% yield. Elemental analysis and AT-IR data support the formation of the expected complex. Our efforts to obtain the single-crystal X-ray structure of complex 1 were not fruitful.

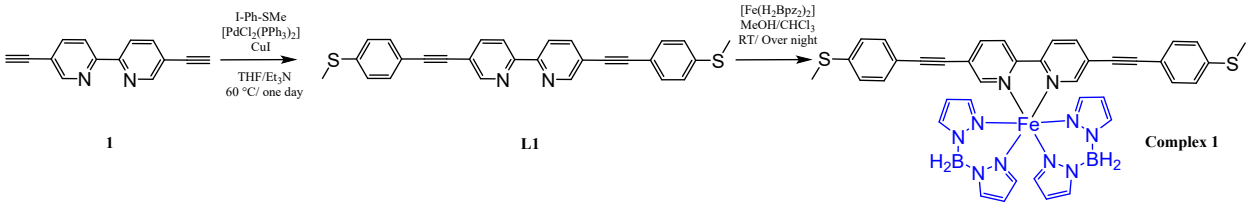

Scheme S1.1. Synthesis of L1 and complex 1.

To a 25 mL of dry and argon purged THF, 4-iodothioanisole (1 g, 4 mmol) was added. To the solution, 5,5'-diethynyl-2,2'-bipyridine (0.408 g, 2 mmol) was added followed by the addition of $[PdCl_2(PPh_3)_2]$ (10 mol%) and CuI (10 mol%). Twenty-five mL of freshly distilled Et_3N was added to the mixture, and the mixture was stirred under argon atmosphere for a day at 60 °C. The reaction mixture was cooled to RT and evaporated to dryness. The solids were washed with 200 mL of dichloromethane (DCM) and filtered. The red DCM solution was washed with water and brine and dried by storing above Na_2SO_4. Column chromatography using silica gel as a stationary phase and 4% MeOH in 96% DCM as eluent yielded the ligand as a pale-yellow solid after three successive attempts.

Yield: 0.172 g (19.2%) ^{1}H NMR (500 MHz, CD_2Cl_2): δ 8.79 (s, 2H), 8.44 (s, 2H), 7.94 (d, *J* = 7.12 Hz, 2H), 7.49 (d, *J* = 8.41 Hz, 2H), 7.24 (d, *J* = 8.41 Hz, 2H), 2.51 (s, 6H). ^{13}C NMR (125 MHz, CD_2Cl_2): δ 131.97, 125.72, 77.65, 77.39, 15.03. Due to the lack of solubility of the ligand, all the expected peaks are not observed in the ^{13}C NMR spectrum. ESI-MS: Calculated for $M+H^+$ = 449.1141; Found = 449.3061. Elemental analysis: Calculated for $C_{28}H_{20}N_2S_2$: C, 74.97; H, 4.49, N, 6.24. Found: C, 73.51, H, 4.46, N, 6.11.

To a solution of iron (II) perchlorate hydrate (0.037 g, 0.1 mmol) in 5 ml of methanol, potassium dihydro(bispyrazolyl)borate (0.0375 g, 0.2 mmol) was added, and the mixture was stirred for 15 min and filtered to remove the precipitated $KClO_4$. This step yields the charge-neutral precursor $[Fe(H_2Bpz_2)_2]$. A solution of ligand (0.0445 g, 0.1 mmol) dissolved in 9 ml of chloroform and 1 ml of methanol was added to the filtrate, and the reaction mixture was stirred overnight under argon protection. The reaction

mixture was filtered, precipitate washed with methanol several times, and dried under vacuum overnight to obtain the complex as a greenish-yello w product.

Yield: 12.7 mg (16%). Elemental Analysis: Calc. for: ($C_{40}H_{36}B_2FeN_{10}S_2 \cdot 0 \cdot 4CHCl_3$) C, 57.35; H, 4.34; N, 16.55; Found: C, 57.36; H, 4.19; N, 15.51. ATR-IR (cm^{-1}): 2408, 2366 ($\nu_{asym.}$ [-BH_2]) 2283, 2222 ($\nu_{sym.}$ [-BH_2]).

S1.2. Synthesis of L2 and attempted preparation of complex 2

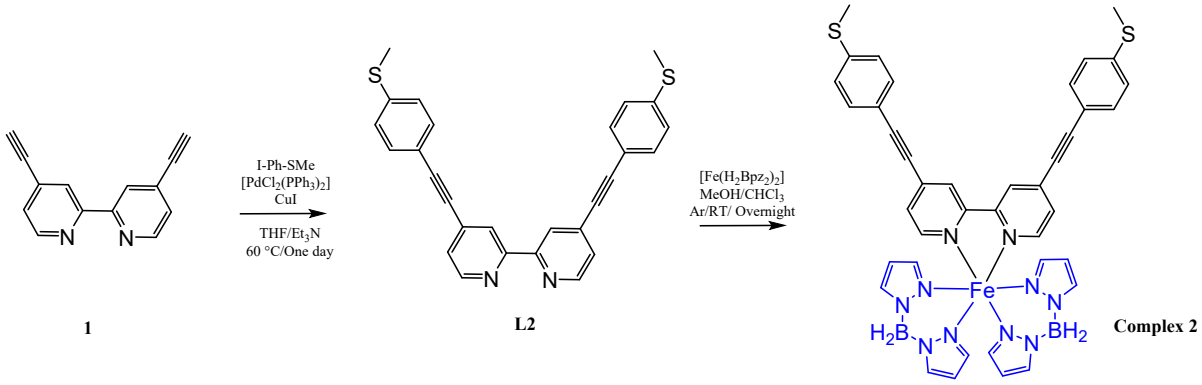

Scheme S1.2. Synthesis of L2 and attempted preparation of complex 2.

Compound 1 was prepared following the procedure reported in the literature.[2]

To a 5 mL of dry and argon purged THF, 4-iodothioanisole (0.5 g, 2 mmol) was added. To the solution, 4,4'-diethynyl-2,2'-bipyridine (0.145 g, 0.72 mmol) was added followed by the addition of [$PdCl_2(PPh_3)_2$] (10 mol%) and CuI (10 mol%). Five mL of freshly distilled Et_3N was added to the mixture, and the mixture was stirred under argon atmosphere for a day at 60 °C. The reaction mixture was cooled to RT and evaporated to dryness. The solids were washed with 100 mL of dichloromethane (DCM) and filtered. The red DCM solution was washed with water and brine and dried by storing above Na_2SO_4. Column chromatography using silica gel as a stationary phase and 4% methanol and 96% DCM as eluent yielded the ligand as a pale cream solid after two successive attempts.

Yield: 0.089 g (29%) ^{1}H NMR (500 MHz, $CDCl_3$): δ 8.67 (d, *J* = 7.12 Hz, 2H), 7.23 (d, *J* = 8.3657, 2H), 7.47 (d, *J* = 8.3487 Hz, 2H), 7.39 (d, *J* = 1.3227 Hz, 2H), 7.24 (d, *J* = 4.9543 Hz, 2H), 2.51 (s, 6H). ^{13}C NMR (125 MHz, $CDCl_3$): δ 155.8, 149.4, 140.9, 132.7, 132.3, 125.8, 125.5, 123.3, 118.4, 94.2, 87.3, 15.3. ESI-MS: Calculated for M+H$^+$ = 449.1141; Found = 449.0954. Elemental analysis: Calculated for $C_{28}H_{20}N_2S_2$: C, 74.97; H, 4.49, N, 6.24. Found: C, 75.05, H, 5.18, N, 5.75.

We have attempted to prepare complex 2 following the procedure established for the preparation of complex 1. However, no satisfactory elemental analysis data were obtained for complex 2. Therefore, we restrain from reporting further data of complex 2.

Ideally, charge neutral complexes belonging to [Fe(H_2Bpz_2)$_2$(L)] family are prepared by taking advantage of their insolubility in polar solvents such as methanol. Addition of a bipyridine-based ligand dissolved either in methanol, a minimum amount of chloroform, or chloroform:methanol solvent mixture results in the precipitation of the expected complex.[3,4] Such precipitation requires good solubility of the bipyridine-based ligands so that the reaction mixture remains polar enough to aid the precipitation of the charge neutral [Fe(H_2Bpz_2)$_2$(L)] complexes. Due to the low solubility of the ligands 1 and 2 in common organic solvents, it was necessary to use chloroform:methanol solvent mixture in a 9:1 ratio to dissolve them. While a precipitate of complex 1 was obtained, the good solubility of complex 2 in chloroform methanol solvent mixture hindered the precipitation of it. Our attempts to obtain powder and crystalline forms of complex 2 upon slow evaporation of the reaction mixture was not successful, and elemental analysis data of the obtained powder was not satisfactory to unambiguously prove the identity of complex 2.

In order to obtain more insight into the stability of complex 2 stability, we calculate the standard Gibbs free energy (G) of formation of the complex as well as its precursors (Ligand 2 and Fe(II)(H_2Bpz_2)$_2$), to then compute the complex's ΔG of formation according the following equation:

$$\Delta G = G_{complex} - (G_{Fe(II)\left(H_2Bpz_2\right)_2} + G_{Ligand})$$

In addition, we also evaluate ΔG for complex 1 to check the consistency of our results. The geometry optimization and vibrational frequencies calculations on the systems, were performed using the ORCA software package[5], by means of the Perdew–Burke–Ernzerhof (PBE)[6] exchange-correlation (XC) functional, and representing all atoms with a def2-TZVP[7] basis set, with the exception of the Fe ion, where a larger def2-QZVPP basis set was employed.

The computed ΔG of formation of each complex is presented in Table SX

Table SX. Obtained values for ΔG of formation (kcal/mol) on each complex.

Complex	ΔG
1	-18.61
2	-19.73

It can be observed that ΔG of formation of both complexes is negative, thus, indicating that both are thermodynamically stable. Also, both systems show almost the same ΔG value with an energy difference

of 1 kcal/mol, which suggests that both complexes could be synthesized. Unfortunately, we were unable to obtain complex 2 in its pure form.

S2. Isolated complexes calculations

S2.1. CASSCF/NEVPT2 active space

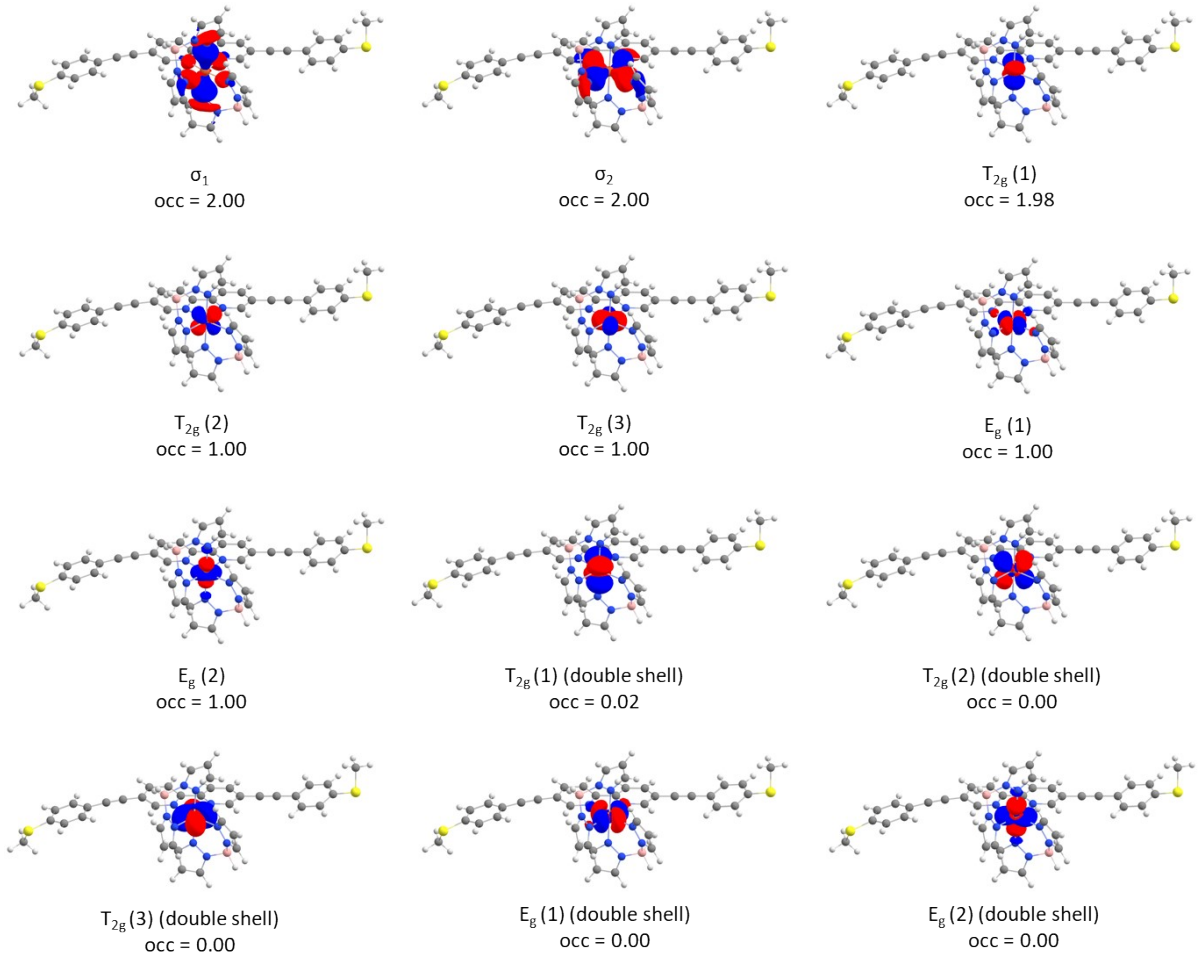

Figure S2.1.1. Natural orbitals obtained from a CAS(10.12) calculation with complex 1 in the HS configuration.

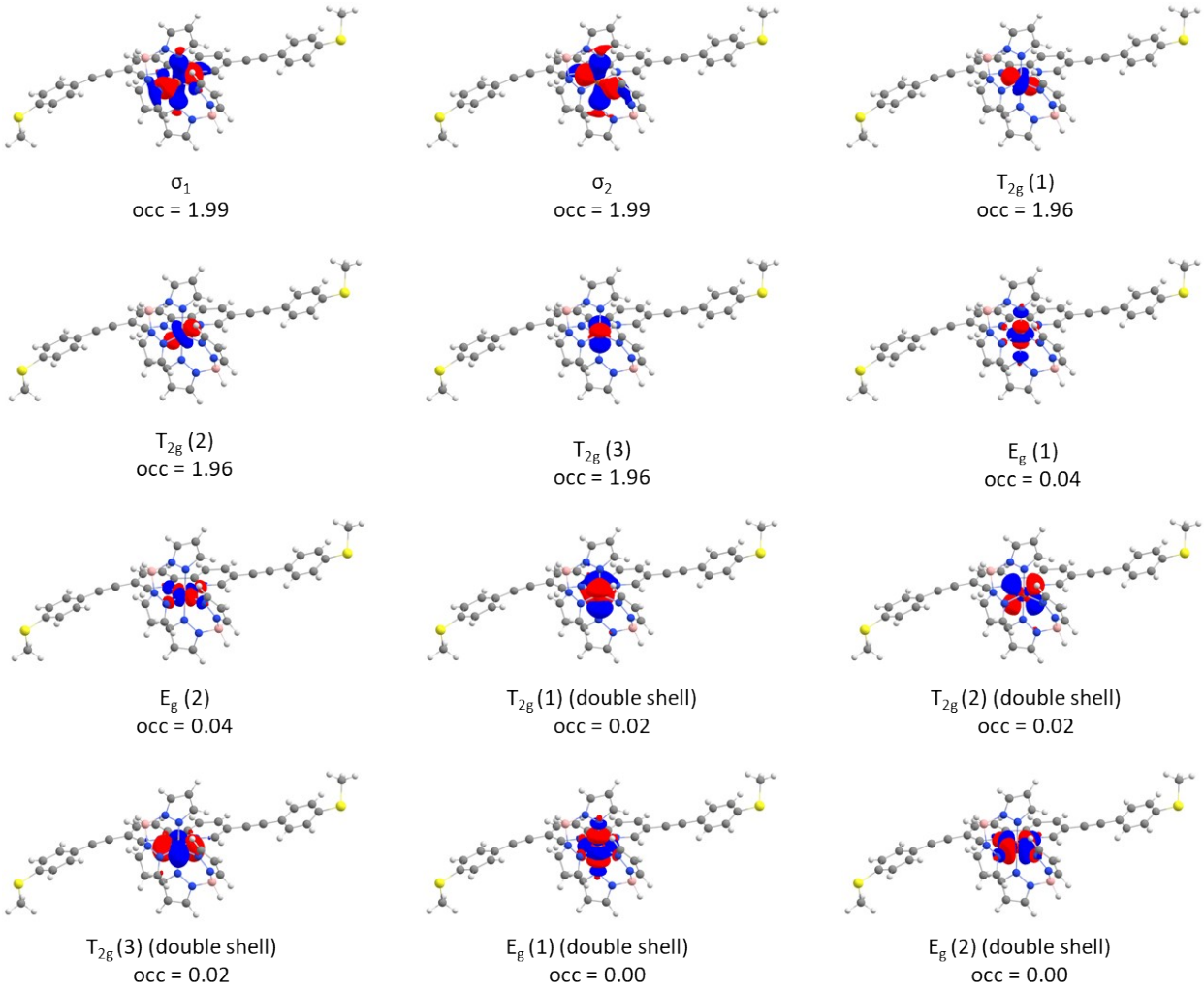

Figure S2.1.2. Natural orbitals obtained from a CAS(10.12) calculation with complex 1 in the LS configuration.

S2.2. Electronic and magnetic properties of the complex

Employing the geometry adopted by complex 1 and 2 in the molecular junction architectures for each spin state (see Computational Details Section), we determined the energy difference between HS (S=2) and LS (S=0) configurations of the isolated compounds ($\Delta E = E_{HS}-E_{LS}$), by performing DFT and WFT calculations. In addition, we also calculated the HS-LS energy gap in the $[Fe(H_2Bpz_2)_2(bipy)]$ reference complex 3, whose transition temperature (Tc = 160K), enthalpy (ΔH = 13.4 kJ mol^{-1}), and entropy (ΔS = 83.9 J mol^{-1} K^{-1}) variations upon SCO have been experimentally determined.[8] The results of these studies are summarized in Table S1. It is important to note that the geometry used for complex 3 in our calculations is the same adopted by complex 1 in the junction once the L1 ligands are removed. No further structure optimization has been performed, due this could affect the HS-LS energy difference when compared to the available experimental data for complex 3 in the bulk.

Table S1. Computed energy differences ($\Delta E = E_{HS}-E_{LS}$) (in kJ/mol) between the HS and LS configurations of complexes 1, 2, and 3.

Methodology	$\Delta E = E_{HS}-E_{LS}$ Complex 1	Complex 2	Complex 3
DFT (QuantumATK)			
PBE	87.7	92.2	90.8
rPBE	52.9	57.4	56.7
DFT (ORCA)			
PBE	93.5	97.1	94.7
rPBE	42.4	45.7	44.4
WFT (ORCA)			
CAS(10.12)/NEVPT2	13.2	7.1	11.3

In the first place, it can be observed that the energy difference between the HS and LS configurations on the three studied complexes, obtained through the QuantumATK and ORCA codes, do not show significant differences, despite the underlying differences in the DFT implementation in these two codes. The calculations performed with the PBE and rPBE functionals predict that the complex's LS configuration is more stable, although the HS-LS gap obtained through the rPBE is nearly 50% lower than the PBE ones. This last behavior has been reported in studies performed on similar Fe SCO complexes, where the rPBE values are closer to the experimental values. Although the HS-LS gaps computed with the rPBE and PBE functionals show a substantial difference, both yielded similar frontier orbital energies in both the LS and HS configurations of the complexes (Figure S2.2.1). This last fact supports the use of the PBE functional in the transport properties calculations, since the energy and composition of the frontier orbitals are crucial factors in the resulting transport properties of the molecular junction. The HS-LS gap evaluated through DFT methods is similar for the three studied complexes. Nevertheless, a tendency is observed, independent of the employed software or XC functional, where complex 1 shows the smallest HS-LS energy gap, followed by complex 3 and finally, complex 2 presents the largest energy gap. Finally, WFT calculations performed on the three complexes yield markedly reduced ΔE values compared to the DFT values. This fact is in line with previous works devoted to the theoretical study of SCO complexes,[9] where a significant overestimation of the calculated ΔE values is reported when DFT-based methods are employed, compared with the available experimental transition enthalpy values.

Table S2. Calculated components of the dipole moment (in a.u.) of the studied complexes, using the CASSCF/NEVPT2 methodology.

	Complex 1			Complex 2			Complex 3		
	x	y	z	x	y	z	x	y	z
HS	-0.33	2.92	0.05	-0.22	3.11	0.08	-0.07	2.75	0.04
LS	0.09	2.78	0.11	-0.18	2.97	-0.02	-0.17	2.56	0.09

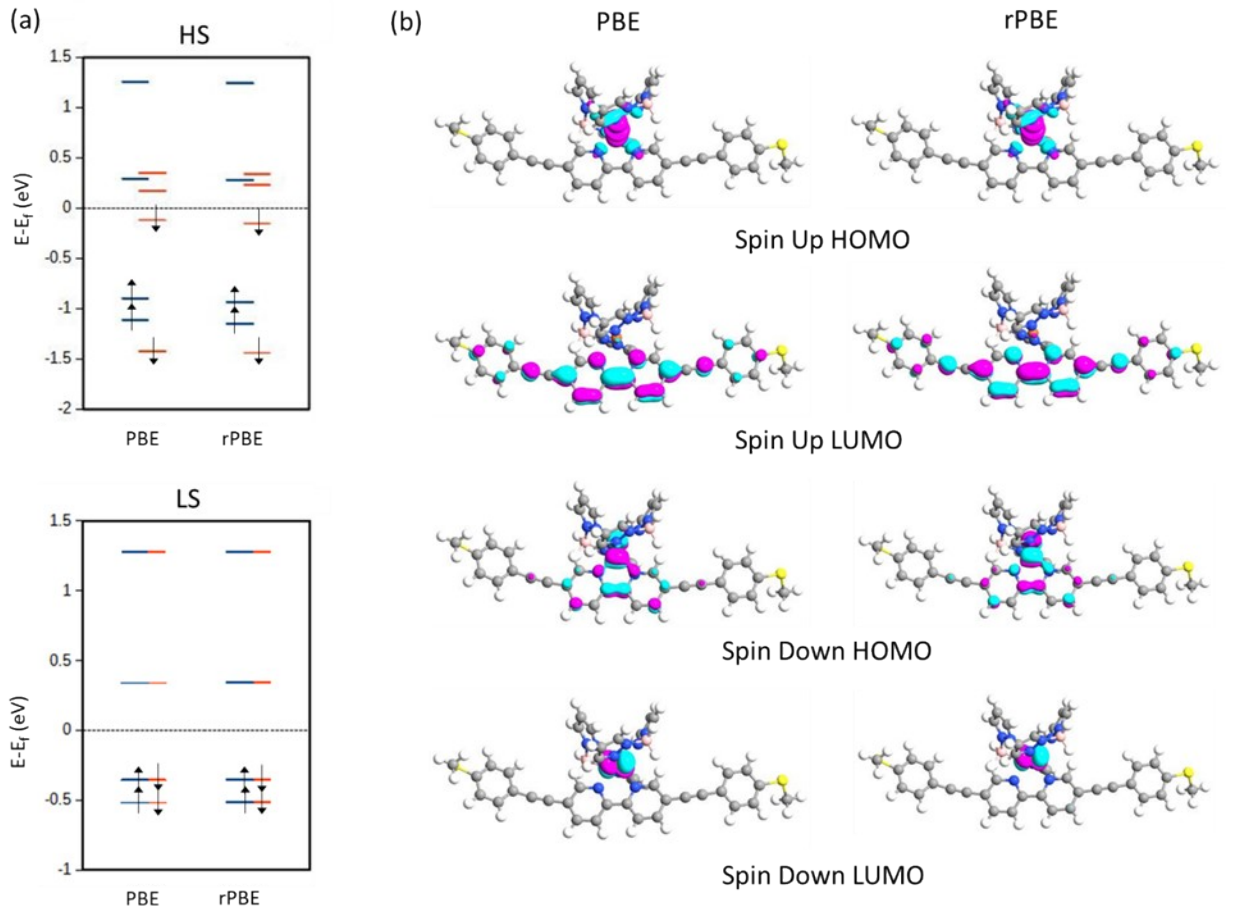

Figure S2.2.1. (a) Frontier molecular orbitals diagram of complex 1 in both its high spin (HS) and low spin (LS) configurations. (b) Plot of the most relevant frontier orbitals for the complex in the HS configuration. Computations were performed using the QuantumATK package and employing the PBE and rPBE exchange-correlation functionals.

S3. Transport properties of Complex 1 and 2 in HS configuration at zero bias

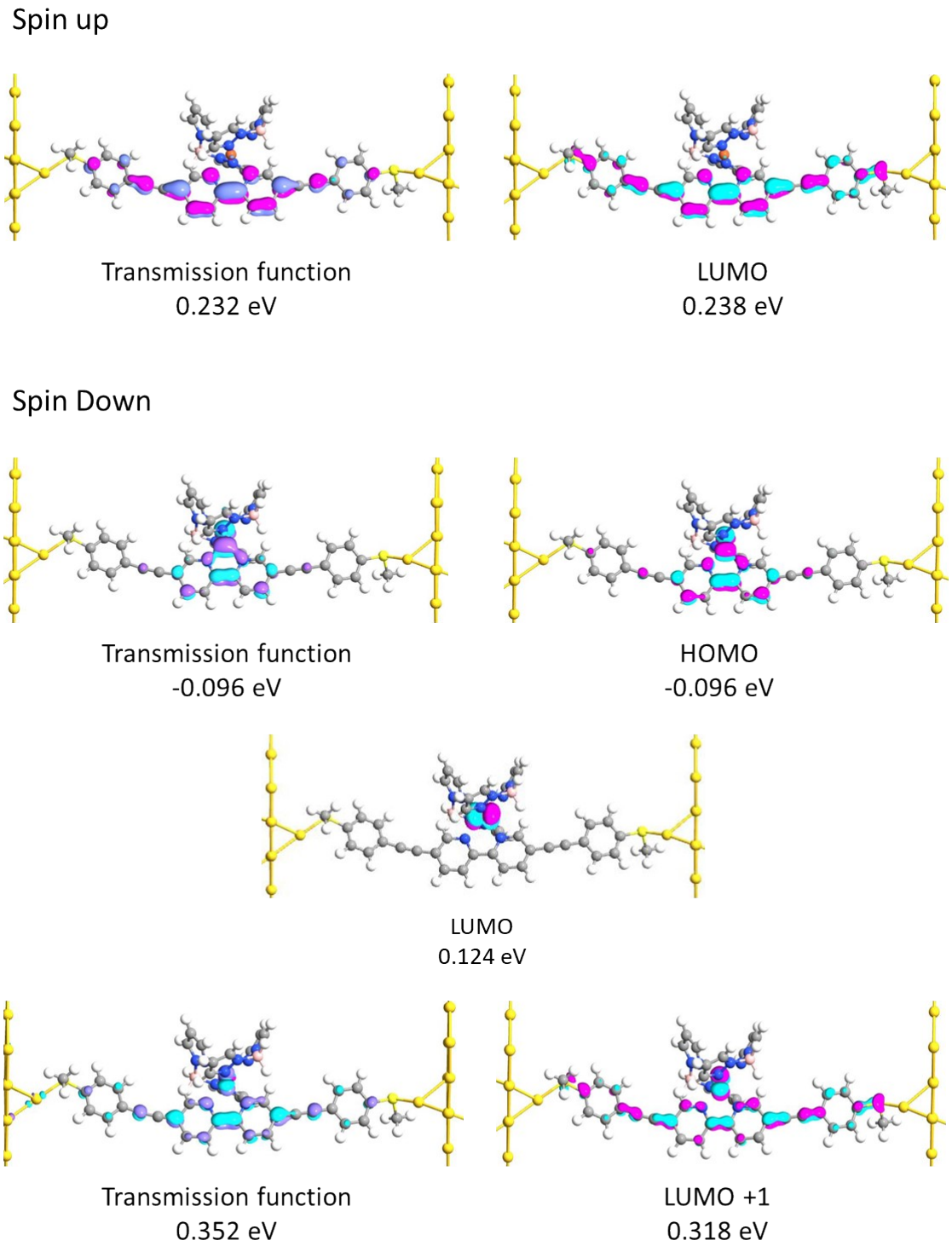

Figure S3.1. Relevant transmission eigenfunctions and frontier orbitals computed in the junction featuring complex 1 in the HS configuration.

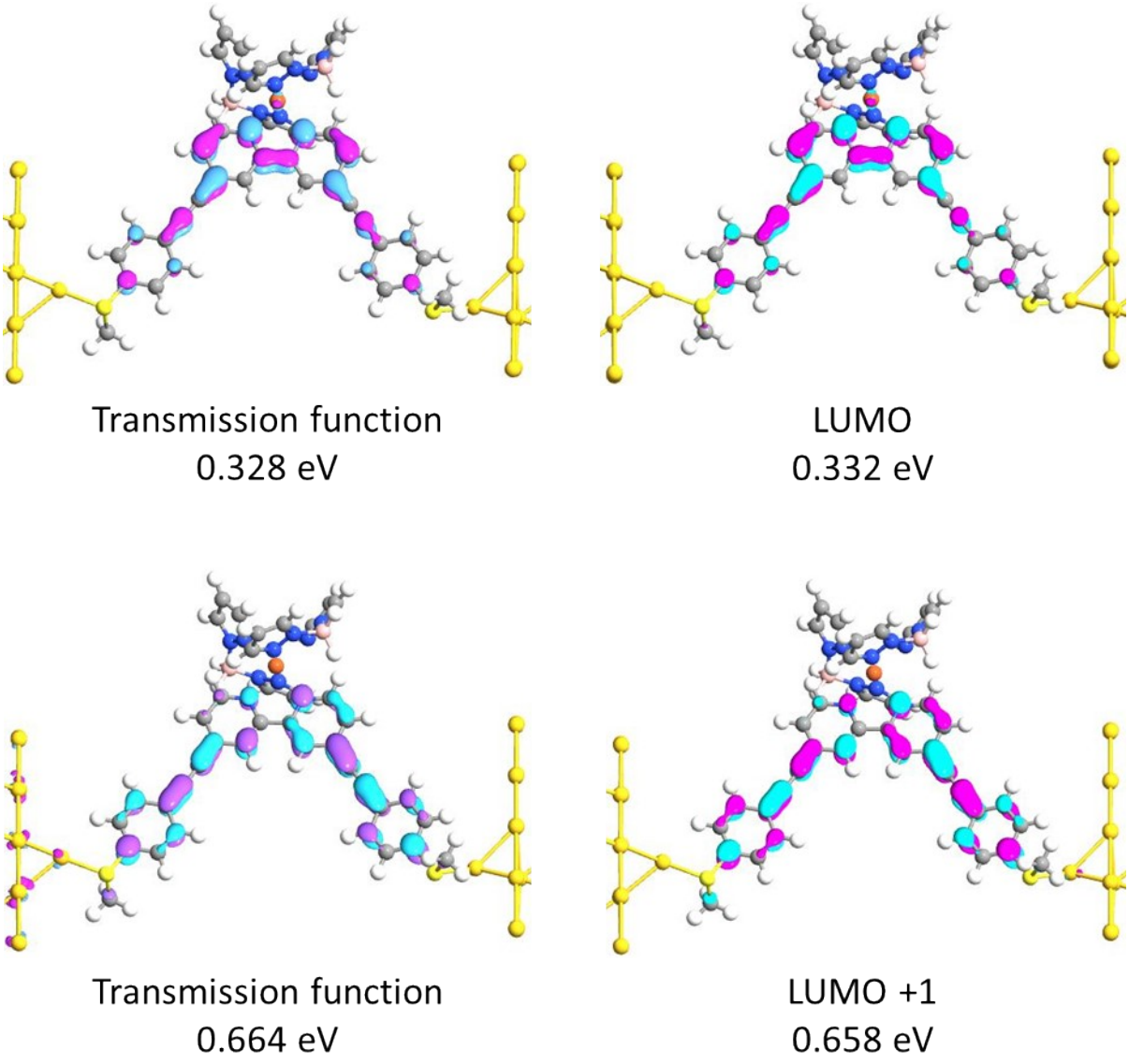

Figure S3.2. Relevant spin-up transmission eigenfunctions and frontier orbitals computed in the junction featuring complex 2 in the HS configuration.

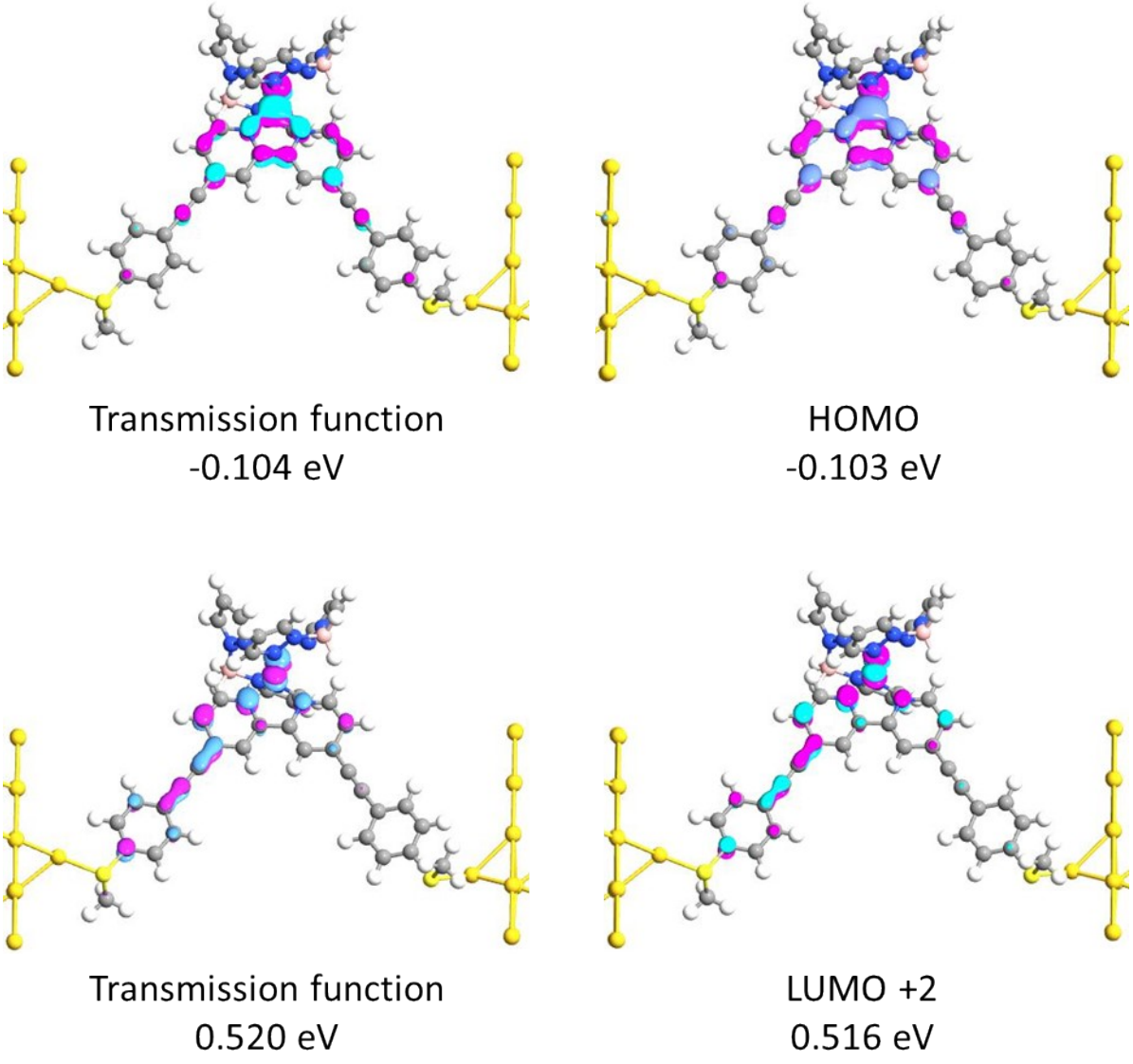

Figure S3.3. Relevant spin-down transmission eigenfunctions and frontier orbitals computed in the junction featuring complex 2 in the HS configuration.

S4. Transport properties of Complex 1 and 2 in HS configuration with an applied bias voltage

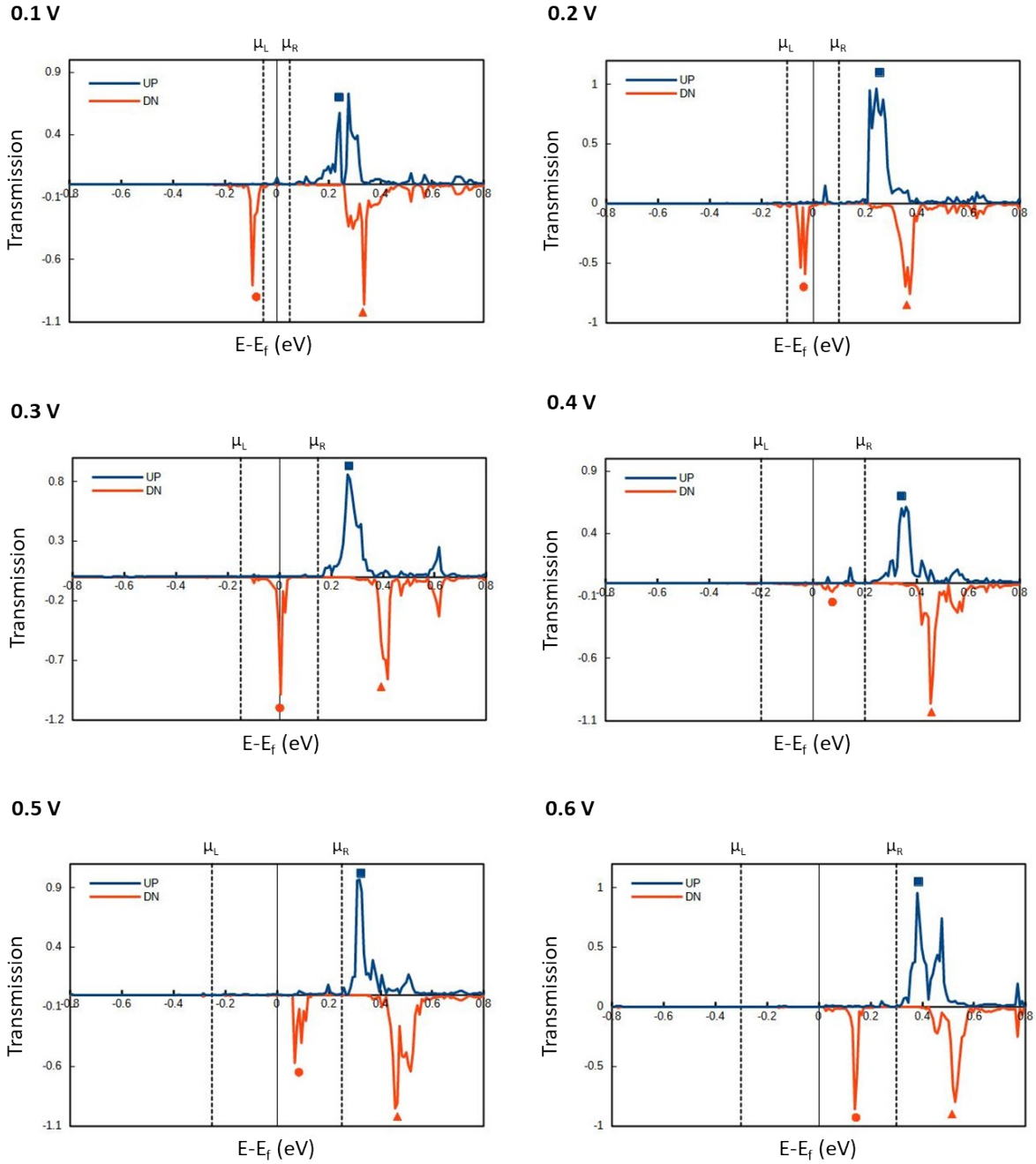

Figure S4.1. Transmission spectrum of the junction utilizing the complex 1 HS configuration as active element, when different bias voltage values are applied to the electrodes. Blue (red) circles represent the position of the spin-up (spin down) HOMO, squares the spin-up (spin down) LUMO, and triangles the spin-up (spin down) LUMO +1. μ_L and μ_R indicate the position of the left (L) and right (R) electrode chemical potentials.

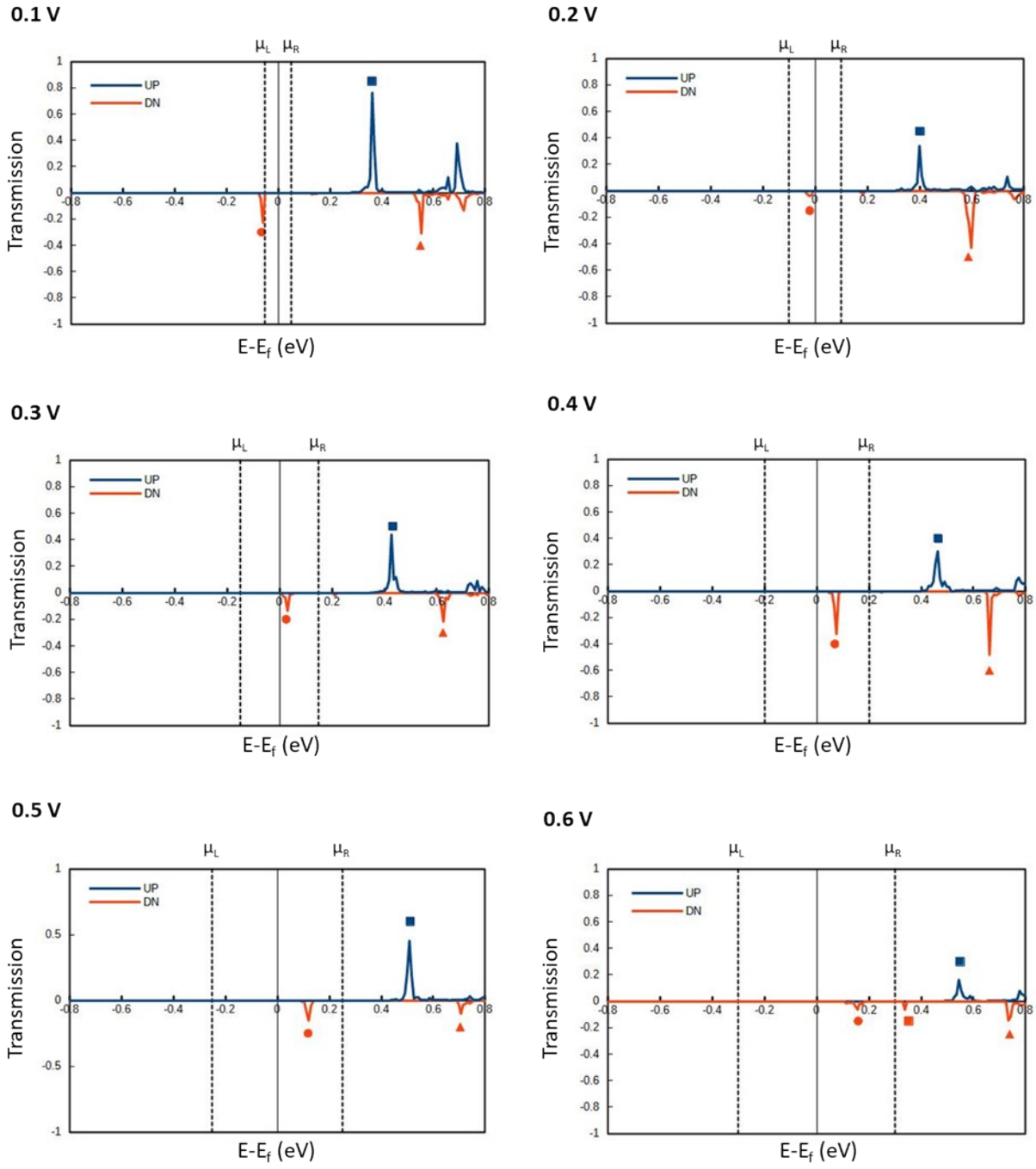

Figure S4.2. Transmission spectrum of the junction utilizing complex 2 in the HS configuration as active element, when different bias voltage values are applied to the electrodes. Blue (red) circles represent the position of the spin-up (spin down) HOMO, squares the spin-up (spin down) LUMO, and triangles the spin-up (spin down) LUMO +2. μ_L and μ_R indicate the position of the left (L) and right (R) electrode chemical potentials.

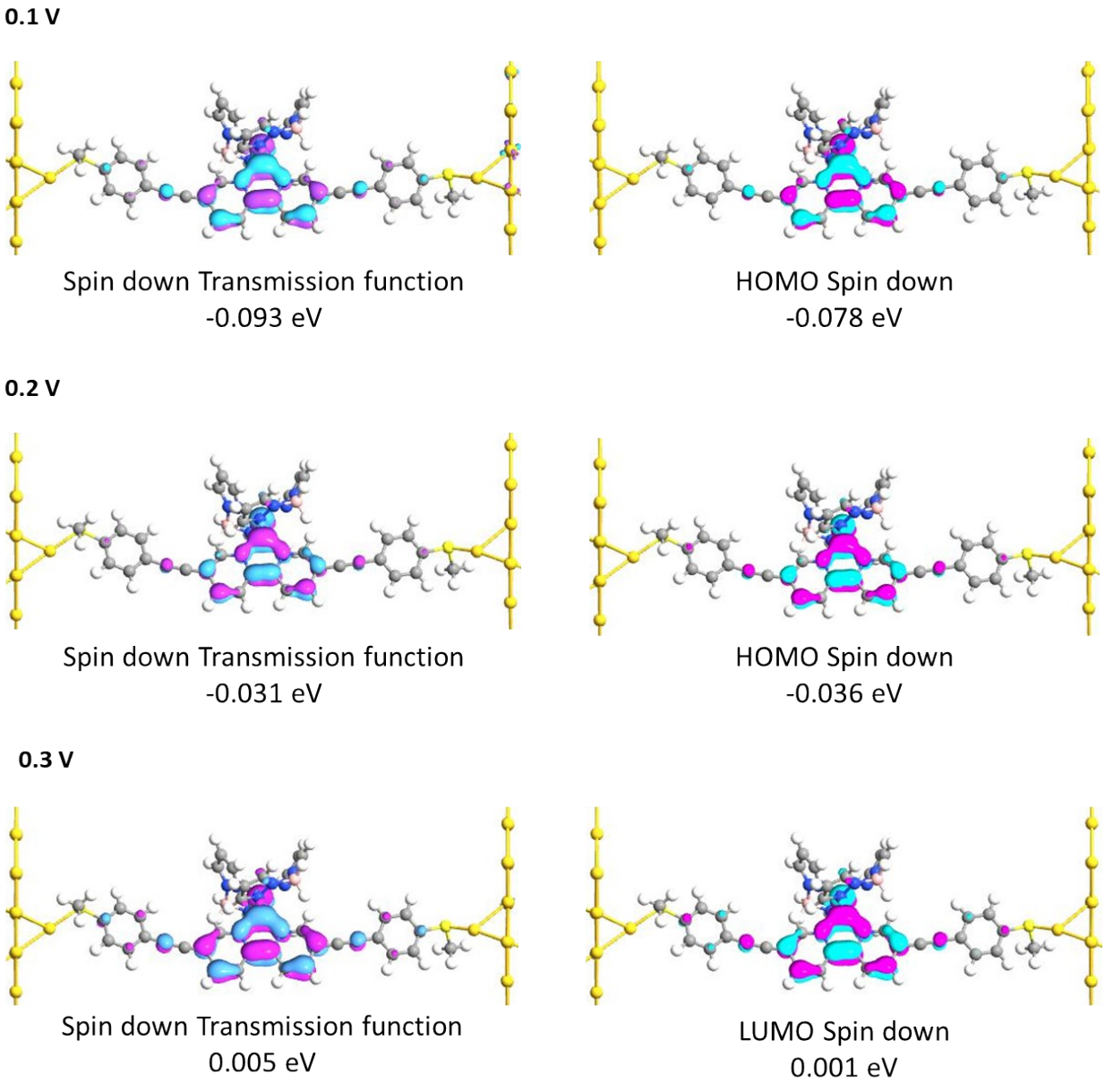

Figure S4.3. Relevant transmission eigenfunctions and frontier orbitals computed in the junction featuring complex 1 in the HS configuration, when a voltage bias from 0.1 to 0.3 V is applied between the electrodes.

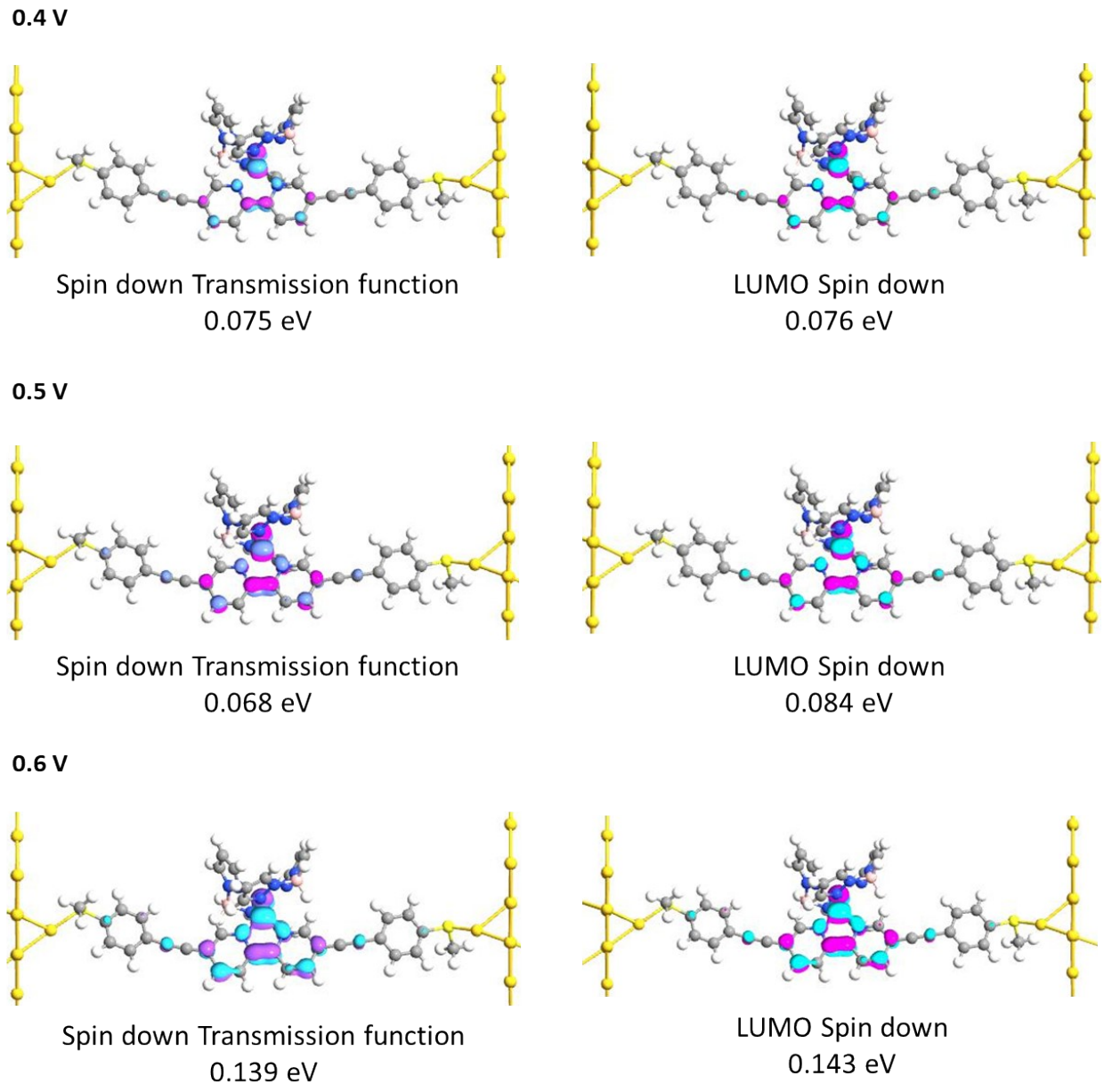

Figure S4.4. Relevant transmission eigenfunctions and frontier orbitals computed in the junction featuring complex 1 in the HS configuration, when a voltage bias from 0.4 to 0.6 V is applied between the electrodes.

S5. Transport properties of Complex 1 and 2 in LS configuration at zero bias

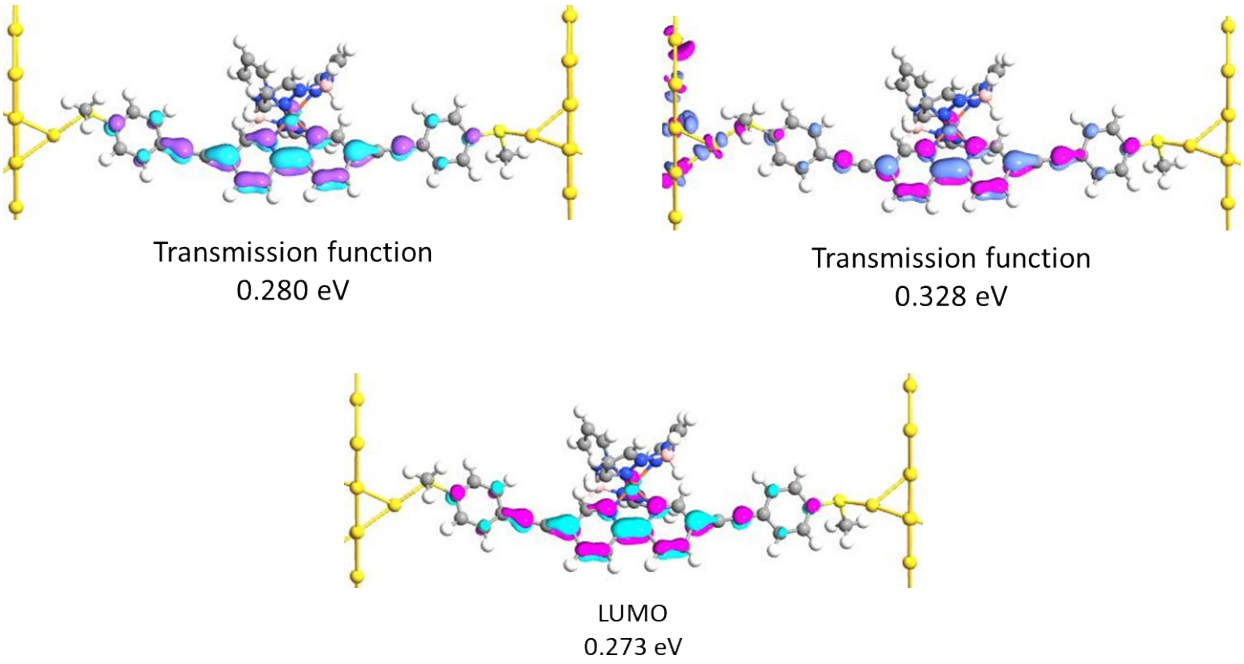

Figure S5.1. Relevant transmission eigenfunctions and frontier orbitals computed in the junction featuring the complex 1 in the LS configuration.

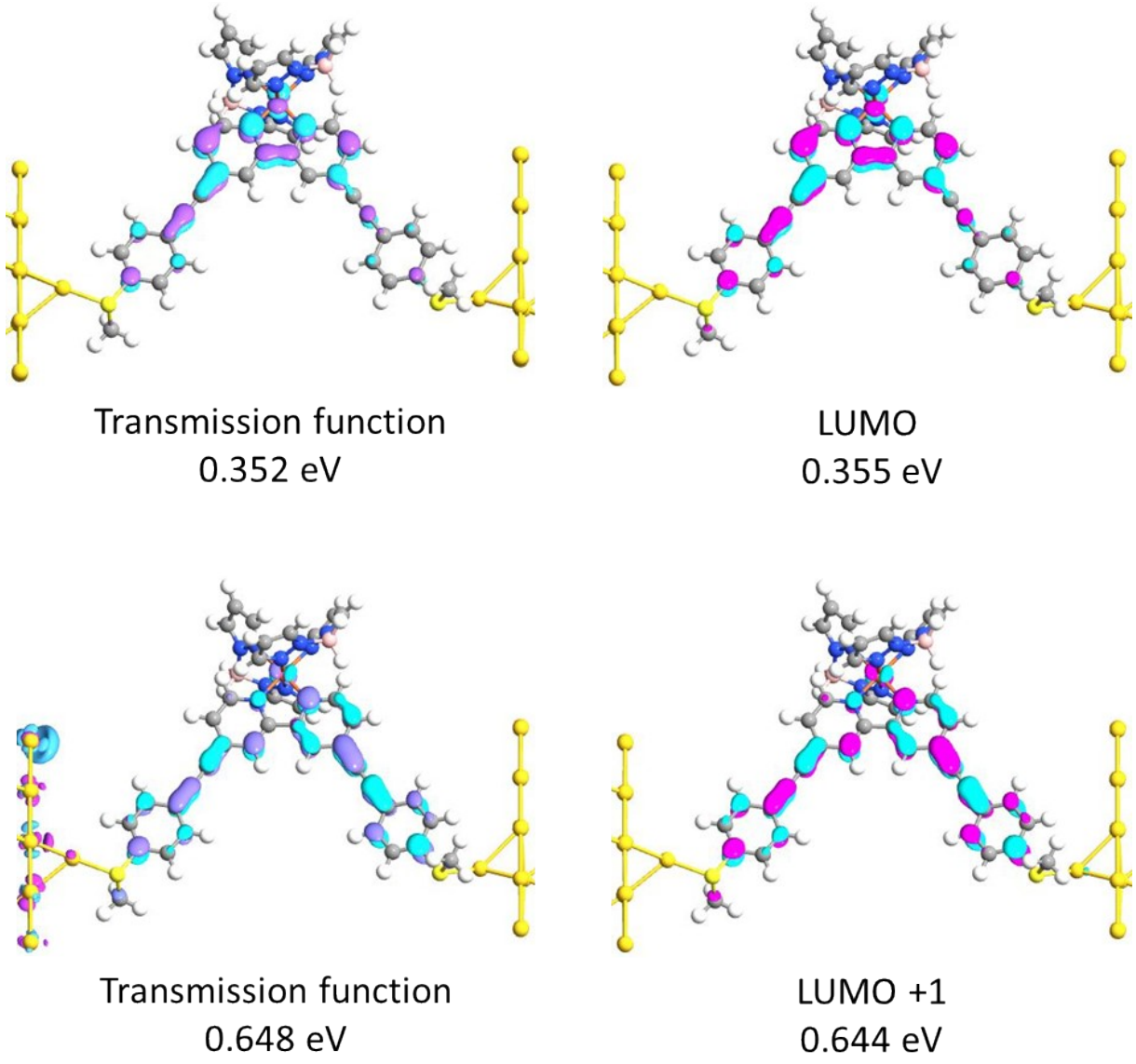

Figure S5.2. Relevant transmission eigenfunctions and frontier orbitals computed in the junction featuring the complex 2 in the LS configuration.

S6. Transport properties of ligands L1 and L2 at zero bias

Spin Up/Down

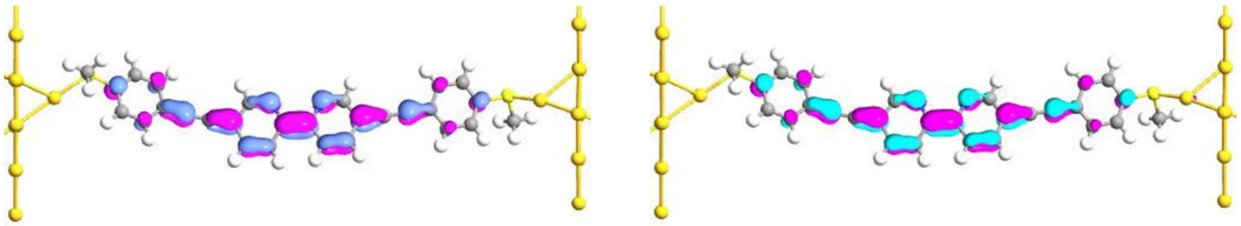

Transmission function
0.384 eV

LUMO
0.382 eV

Figure S6.1. Relevant transmission eigenfunctions and frontier orbitals computed in the junction featuring the ligand L1.

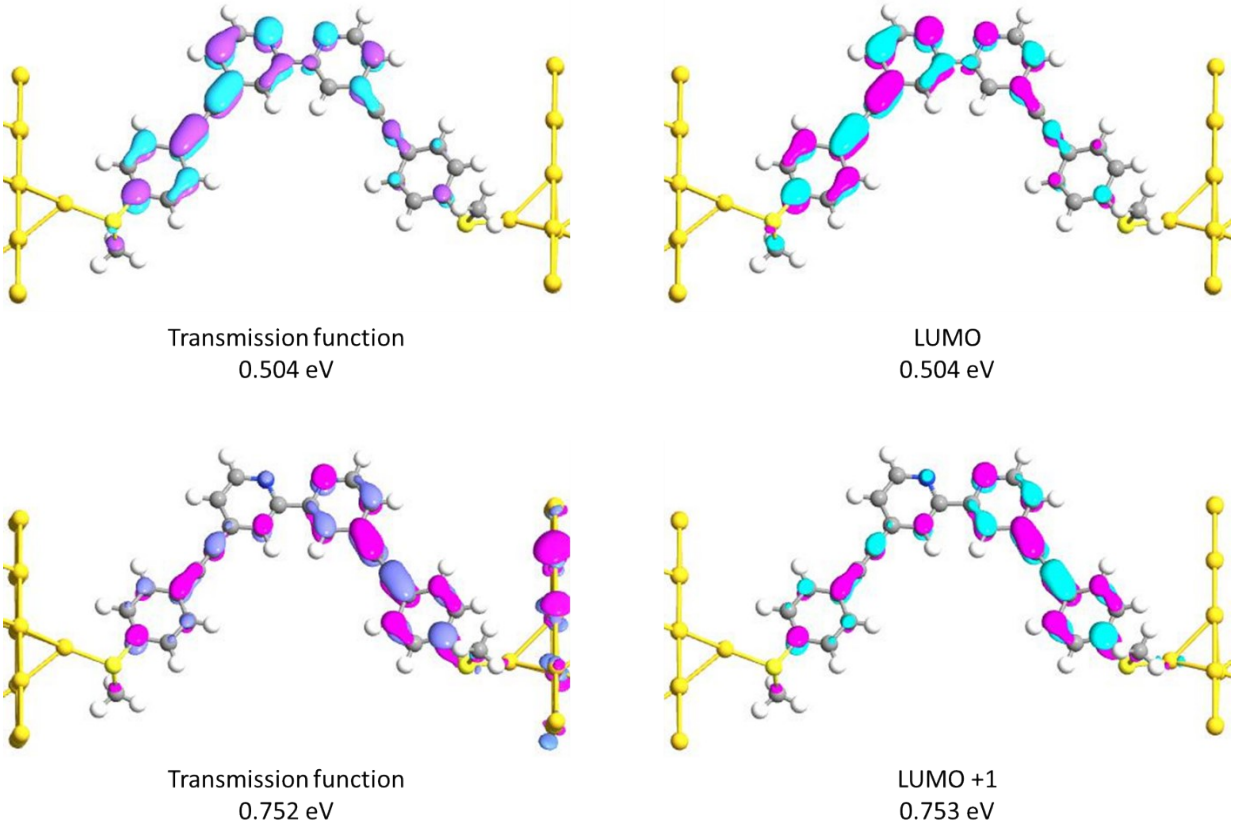

Figure S6.2. Relevant transmission eigenfunctions and frontier orbitals computed in the junction featuring the ligand L2.

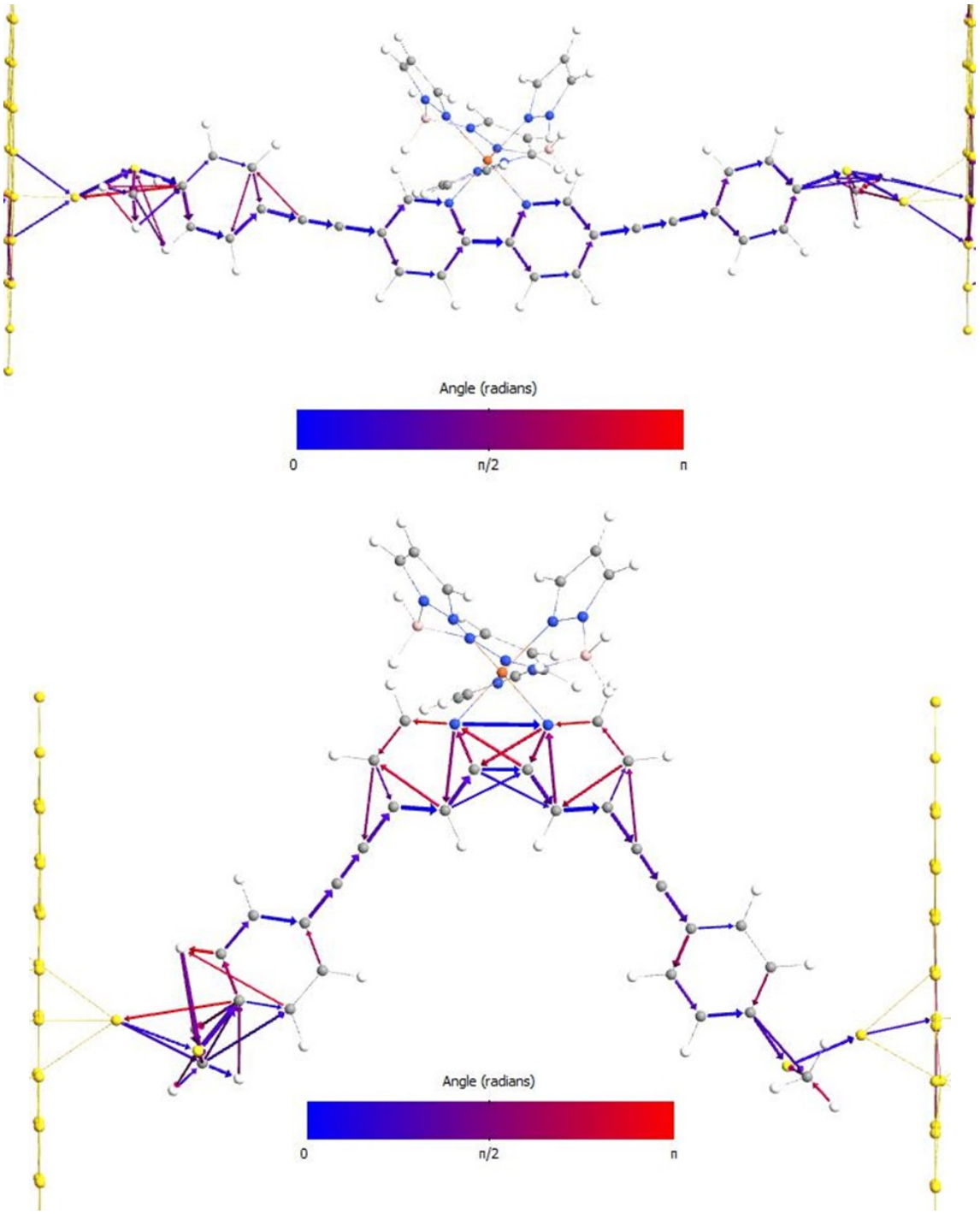

Figure S6.3. Transmission pathways corresponding to the LUMO resonances of complex 1 (top) and 2 (bottom) in LS configuration. The color scale represents the direction of the transport; blue (0) means transport from left to right electrode, (π/2) perpendicular to the electrodes, and (π) from right to left. Note that in the picture only the contributions originated from the left electrodes were included, so the right-left transmission is mainly the product of wave reflection.

S7. References

(1) Grosshenny, V.; Romero, F. M.; Ziessel, R. Construction of Preorganized Polytopic Ligands via Palladium-Promoted Cross-Coupling Reactions. *The Journal of Organic Chemistry* **1997**, *62* (5), 1491-1500. DOI: 10.1021/jo962068w.

(2) Rest, C.; Philips, D. S.; Dünnebacke, T.; Sutar, P.; Sampedro, A.; Droste, J.; Stepanenko, V.; Hansen, M. R.; Albuquerque, R. Q.; Fernández, G. Tuning Aqueous Supramolecular Polymerization by an Acid-Responsive Conformational Switch. *Chemistry – A European Journal* **2020**, *26* (44), 10005-10013. DOI: https://doi.org/10.1002/chem.202001566.

(3) Kumar, K. S.; Studniarek, M.; Heinrich, B.; Arabski, J.; Schmerber, G.; Bowen, M.; Boukari, S.; Beaurepaire, E.; Dreiser, J.; Ruben, M. Engineering On-Surface Spin Crossover: Spin-State Switching in a Self-Assembled Film of Vacuum-Sublimable Functional Molecule. *Advanced Materials* **2018**, *30* (11), 1705416, https://doi.org/10.1002/adma.201705416. DOI: https://doi.org/10.1002/adma.201705416 (acccessed 2022/09/27).

(4) Kuppusamy, S. K.; Spieker, L.; Heinrich, B.; Salamon, S.; Gruber, M.; Wende, H.; Ruben, M. Bistable spin-state switching characteristic of a charge-neutral iron(II) complex. *ChemRxiv* **2022**, *This content is a preprint and has not been peer-reviewed.* DOI: 10.26434/chemrxiv-2022-9mtbs.

(5) Neese, F. The ORCA program system. *Wiley Interdisciplinary Reviews: Computational Molecular Science* **2012**, *2* (1), 73-78. DOI: 10.1002/wcms.81 (acccessed 2018/12/17).

(6) Perdew, J. P.; Burke, K.; Ernzerhof, M. Generalized Gradient Approximation Made Simple [Phys. Rev. Lett. 77, 3865 (1996)]. *Physical Review Letters* **1997**, *78* (7), 1396-1396. DOI: 10.1103/PhysRevLett.78.1396.

(7) Weigend, F. Accurate Coulomb-fitting basis sets for H to Rn. *Physical Chemistry Chemical Physics* **2006**, *8* (9), 1057-1065, 10.1039/B515623H. DOI: 10.1039/B515623H.

(8) Real, J. A.; Muñoz, M. C.; Faus, J.; Solans, X. Spin Crossover in Novel Dihydrobis(1-pyrazolyl)borate [H2B(pz)2]-Containing Iron(II) Complexes. Synthesis, X-ray Structure, and Magnetic Properties of [FeL{H2B(pz)2}2] (L = 1,10-Phenanthroline and 2,2'-Bipyridine). *Inorganic Chemistry* **1997**, *36* (14), 3008-3013. DOI: 10.1021/ic960965c.

(9) Cirera, J.; Via-Nadal, M.; Ruiz, E. Benchmarking Density Functional Methods for Calculation of State Energies of First Row Spin-Crossover Molecules. *Inorganic Chemistry* **2018**, *57* (22), 14097-14105. DOI: 10.1021/acs.inorgchem.8b01821. Siig, O. S.; Kepp, K. P. Iron(II) and Iron(III) Spin Crossover: Toward an Optimal Density Functional. *The Journal of Physical Chemistry A* **2018**, *122* (16), 4208-4217. DOI: 10.1021/acs.jpca.8b02027. Reiher, M. Theoretical Study of the Fe(phen)2(NCS)2 Spin-Crossover Complex with Reparametrized Density Functionals. *Inorganic Chemistry* **2002**, *41* (25), 6928-6935. DOI: 10.1021/ic025891l.